THE ASTROPHYSICAL JOURNAL, 470:1198–1217, 1996 October 20

THE SCALING LAW BETWEEN ELECTRON TIME-OF-FLIGHT DISTANCES AND LOOP LENGTHS IN SOLAR FLARES

MARKUS J. ASCHWANDEN
Department of Astronomy, University of Maryland, College Park, MD 20742; markus@astro.umd.edu
TAKEO KOSUGI
National Astronomical Observatory, Mitaka, Tokyo 181, Japan
HUGH S. HUDSON
Institute for Astronomy, University of Hawaii, Honolulu, HI 96822
MEREDITH J. WILLS
Harvard-Smithsonian Center for Astrophysics, 60 Garden Street, Cambridge, MA 02138
AND
RICHARD A. SCHWARTZ
Hughes STX, NASA Goddard Space Flight Center, Code 682, Greenbelt, MD 20771
Received 1996 April 3; accepted 1996 May 10

ABSTRACT

From the complete data set of solar flares simultaneously observed with the Burst and Transient Source Experiment (BATSE) on board the *Compton Gamma Ray Observatory* (*CGRO*) in the high–time resolution mode (64 ms) and the Hard X-ray Telescope (HXT) on board *Yohkoh*, we were able to determine the electron time-of-flight (TOF) distance l' and the flare loop geometry in 42 events. The electron TOF distances were determined from time delays (of $\approx$10–100 ms) of hard X-ray (HXR) pulses (measured in 16 channel spectra over $\approx$20–200 keV), produced by the velocity difference of the HXR-producing electrons. The flare loops were mostly identified from double footpoint sources in $\gtrsim$30 keV HXT images, with radii in the range $r = 3000$–25,000 km. We find a scaling law between the electron TOF distance l' and the flare loop half-length $s = r(\pi/2)$, having a mean ratio (and standard deviation) of $l'/s = 1.4 \pm 0.3$. In five flares, we observe coronal $\gtrsim$30 keV HXR sources of the Masuda type in the cusp region above the flare loop and find that their heights are consistent with the electron TOF distance to the footpoints. These results provide strong evidence that particle acceleration in solar flares occurs in the cusp region above the flare loop and that the coronal HXR sources discovered by Masuda et al. are a signature of the acceleration site, probably controlled by a magnetic reconnection process.

Subject headings: acceleration of particles — radiation mechanisms: nonthermal — Sun: corona — Sun: flares — Sun: X-rays, gamma rays

1. INTRODUCTION

The kinematics of electrons in solar flares can be probed by time-of-flight measurements using the energy-dependent timing of hard X-ray (HXR) pulses. For typical solar flare spectra, HXRs in the energy range of 25–250 keV are mostly produced by electrons with kinetic energies of $\approx$50–500 keV, which have relativistic velocities in the range of $\beta = v/c \approx 0.4$–0.9, leading to flight time differences up to a factor of 2. We use this method to determine the spatial location of the so far elusive electron acceleration sites in solar flares.

Three prerequisites are required for such a kinematic experiment: (1) the identification of the electron energy loss site, (2) the measurement of time differences for particles with different speeds, and (3) the verification of a simultaneous start at the departure place. The first requirement can easily be met by selecting flares with hard X-ray footpoint emission (Hoyng et al. 1981; Duijveman, Hoyng, & Machado 1982; Takakura, Tanaka, & Hiei 1984; Sakao 1994). This localizes the energy loss site of precipitating electrons inside a chromospheric layer with a depth of $\lesssim$ 2500 km, in the framework of the thick-target model (Brown 1971; Hudson 1972; Emslie 1978, 1983). The second requirement, the feasibility of time difference measurements between HXR-producing electrons of different speeds (or kinetic energies), has been first demonstrated with *Compton Gamma Ray Observatory* (*CGRO*) data in Aschwanden, Schwartz, & Alt (1995b, hereafter Paper I), and also with *Solar Maximum Mission* (*SMM*) data in Aschwanden et al. (1995a). It was found that only the rapid fluctuations (on timescales of $\lesssim$1 s) of the HXR flux, which generally account for only $\lesssim$10% of the total HXR flux, contain information on directly precipitating electrons suitable for time-of-flight measurements, while the smoothly varying, gradual HXR flux has an opposite timing and is probably dominated by trapping effects. The accuracy of such relative delay measurements can exceed the instrumental time resolution of the HXR detector, for temporally resolved pulses with a high signal-to-noise ratio (Aschwanden & Schwartz 1995, hereafter Paper II). For a proper determination of the electron time-of-flight (TOF) distance, the convolution of a time-dependent electron injection spectrum with the bremsstrahlung cross section and the instrumental response function needs to be inverted. This task has been numerically simulated for power-law spectra with a high-energy cutoff (Aschwanden & Schwartz 1996, hereafter Paper III). A first comparison of an electron TOF distance with the geometry of an observed flare loop has been performed for a Masuda-type flare (Masuda 1994a) on 1992 January 13 (Aschwanden et al. 1996a, hereafter Paper IV). The third requirement is the inference of a simultaneous start time for electrons with different energies. Intuitively, it

is expected that the injection of electrons onto a magnetic field line (that connects with the flare loop footpoints) should exhibit an energy dependence that is in some relation to the finite acceleration time, estimated to be of similar order of magnitude as electron propagation times in flare loops (see, e.g., Holman 1985; LaRosa et al. 1996; Miller, LaRosa, & Moore 1996). However, detailed fits of various acceleration models to HXR time delay measurements, with uncertainties of less than a few milliseconds for electron energies in the range of 80–800 keV, have failed to explain the observed HXR timing in terms of acceleration times (Aschwanden 1996, hereafter Paper V). In contrast, electron propagation time differences provide excellent fits to the observed delays within the uncertainties of the Poisson noise (Aschwanden et al. 1996b, hereafter Paper VI). It appears, therefore, that electron propagation time differences can fully account for the observed HXR timing, while acceleration times have a negligible role. This result, however, leaves the question open as to whether acceleration times might be substantially smaller (less than a few ms) than expected, or whether electrons are bottled up in the acceleration region until they get injected into the flare loop by a mechanism that does not discriminate between different energies.

After we have clarified the various prerequisites and issues surrounding the significance of electron TOF measurements (see the first five papers in this series), we can proceed to a systematic exploitation of this method. The most accurate measurements can be performed in flares with the highest signal-to-noise ratio in the HXR count rate. This was attempted for the eight largest flares observed with *CGRO*/BATSE and *Yohkoh*/HXT in Paper VI. In this study, we extend the same measurement technique to the complete data set of flares jointly observed with *CGRO*/BATSE and *Yohkoh*/HXT. A total of 140 such flare events were recorded during the period 1991–1995. Based on this comprehensive and representative data set, we establish a scaling law between the electron TOF distance and the flare loop size.

The contents of this paper are as follows: a brief description of the data selection and analysis (§ 2), the geometric projection of TOF distances onto HXR flare images and the resulting scaling law (§ 3), and an interpretation of TOF distances with regard to the localization of electron acceleration sites (§ 4).

2. OBSERVATIONS AND DATA ANALYSIS

We use high–time resolution (64 ms) data from the 16 channel spectra readout in the Medium Energy Resolution (MER) mode from the BATSE detectors on *CGRO* (Fishman et al. 1989, 1992) for HXR delay measurements in the energy range of $\approx$20–200 keV. For comparisons with HXR images, we make use of the four-channel (Lo: 14–23 keV; M1: 23–33 keV; M2: 33–53 keV; Hi: 53–93 keV) images from HXT on *Yohkoh* (Kosugi et al. 1991), which have a nominal resolution of $\gtrsim 5''$, as well as from simultaneous soft X-ray images from SXT on *Yohkoh* (Tsuneta et al. 1991), having a pixel size of 2.″46. Additional details of the instruments and observations are given in the first six papers in this series.

2.1. *Data Selection*

We compiled a complete list of flare events jointly observed by *CGRO* and *Yohkoh*. Further, we restricted our analysis to high–time resolution (64 ms) data and 16 channel spectra, which require a burst-trigger on BATSE and readout in the MER mode, generally lasting for 164 s. On the *Yohkoh* side, we required simultaneous coverage with HXT in the flare mode, which provides HXR images in the three higher energy channels (M1, M2, and Hi). From the overlapping epoch of both spacecraft (from 1991 October to the end of 1995), we identified 140 commonly observed flare events. A breakdown of the excluded and analyzed events is given in Table 1. Of these events, 108 produced useful MER data; the other 32 events are not accessible because of data loss (mainly during 1992–1995 due to overwriting after the tape recorders on *CGRO* failed) or are corrupted by incomplete readout or pulse pile-up effects.

2.2. *CGRO Data Analysis*

The HXR timing measurements were performed according to the same method as described in Papers II, III, IV, V, and VI. A first preparatory step is the discrimination between the *pulsed* and the *smooth* component of the HXR flux, which generally have different time delay characteristics, mostly of opposite sign (see Papers V and VI). In the last paper (Paper VI), we developed a filter technique using the fast Fourier transform (FTT) to separate the two components (with competing time delays) by varying the filter cutoff until the difference in the time delays between the low-pass and high-pass component is maximized. If the delays are of opposite sign, the correct filter timescale t_F can simply be determined from the maximum of the time delay τ as a function of the filter timescale t_F. For this optimization, we repeated the time delay measurements for each flare over a broad range of filter timescales (t_F = 1–10 s).

A necessary condition to attribute HXR time delays to electron propagation time-of-flight differences is that the low-energy electrons must have a positive time delay with respect to the high-energy electrons. This is generally found to be the case for the *pulsed* component (see the first six papers in this series), while the *smooth* component has often a negative delay (Papers V and VI). From our data set of 108 analyzed MER events, we find a total of 61 flares with positive time delays for the low-energy HXR pulses, while 16 flares show negative delays. Thus, about 80% of flares with fine structure (or pulses) qualify for electron time-of-flight measurements, a ratio similar to that found in earlier

TABLE 1

STATISTICS OF ANALYZED FLARE EVENTS

Event Type	Number of Events
Coincident *CGRO*/MER and *Yohkoh*/HXT events	140
Events with unusable *CGRO*/MER data	32
Analyzed *CGRO*/MER events	108
Events with no fine structure or insignificant delay	31
Events with negative delays of fine structure	16
Events with positive delays of fine structure	61
Events with unusable *Yohkoh*/HXT data	9
Events with analyzed *Yohkoh*/HXT data	52 (100%)
1. HXR Double footpoints + cusp source	5 (10%)
2. HXR Double footpoints	22 (42%)
3. HXR Single footpoints, elliptical	14 (27%)
4. HXR Single footpoints, unresolved	4 (8%)
5. HXR Single footpoints, near limb	7 (13%)

statistical studies (Papers I and II). The other 20% of flares with negative time delays of the pulses are interpreted in terms of (thin- or thick-target) energy loss in the coronal part of the flare loop (Paper II) and are not studied here. Also, we identified a total of 31 flares that did not exhibit significant pulse structures or no significant time delays (over the entire range of analyzed filter time scales). This lack of significant time delays or significant fine structure is caused partially by the limitations of the Poisson noise (for flares with low count rates) and partially because the burst-trigger mode missed the main impulsive phase. Under optimum conditions (at high count rates and with full time coverage of the impulsive phase), only a small percentage of flares ($\lesssim 10\%$) show no fine structure at all.

2.3. *Yohkoh HXT Data Analysis*

In the following we concentrate only on the 61 events with significant positive time delays, for which an electron TOF distance could be determined. From this subset, we omit nine events with no suitable HXT data, either because the count rate was too low ($\lesssim 10$ counts s^{-1} SC^{-1}, where SC = subcollimator) or no suitable background time interval was available to produce useful HXR images with the maximum entropy method (MEM). This leaves us with 52 events with suitable *GRO*/MER and *Yohkoh*/HXT data for TOF distance comparisons.

A breakdown of the morphology of the HXT images is given in Table 1: five flares show HXR double footpoints plus an additional HXR cusp source (three of them are limb events of the Masuda type: Masuda 1994a; Masuda et al. 1994, 1995); 22 flares show HXR double footpoints (Sakao 1994); 14 flares show elongated (elliptical) footpoints, an intermediate type between single and double footpoint sources; four flares show single footpoints, located near disk center; and seven flares show single footpoints, located near the limb, which could also be double footpoint sources with unresolved footpoints due to the foreshortening. Thus, our statistics are similar to those of Sakao, who lists 43% double footpoint sources, 28% single footpoint sources, and 28% multiple sources from a sample of 28 analyzed events.

3. RESULTS

The observational parameters of the 52 analyzed events are listed in Table 2 and graphically presented in Figures 1, 2, 3, and 4. We ordered the 52 flare events into five morphological groups and show the measurements of the first three groups in Figures 1, 2, and 3, including all events with measurable footpoint separation, except for the eight flares shown in Paper VI. The analysis procedure is identical to that used in Paper VI, and we show the results in a condensed format in Figures 1, 2, 3, and 4. For each flare event we show four panels: *Yohkoh*/HXT + SXT maps with projected loop geometries (Figs. 1, 2, 3, and 4, *left-hand panels*), a vertical projection of the loop geometry (*second panels*), the HXR delays and the fit of the TOF model (*third panels*), and the dependence of the TOF distance $l'(t_F)$ on the filter timescale (*right-hand panels*). The analyzed time intervals, over which the TOF model was fitted, were mainly dictated by the *CGRO*/MER burst triggers. They cover in most cases the periods of the impulsive flare phase over which fast HXR pulses occur but stop sometimes before the main flare peak. The used FFT filter timescales t_F indicate the optimized values at which the TOF distance l' is measured, defined by the first peak or plateau left-hand side in the function $l'(t_F)$, within a range of filter timescales with acceptable fits of the TOF model (see discussion in Paper VI). The spectral slope γ is computed from a single power-law fit to the average HXR spectrum over the analyzed time interval and is used for the inversion of the TOF distance l' from the measured HXR delays (Paper III). The TOF distance l' is determined from the best fit to the HXR delays (Figs. 1, 2, 3, and 4, *third panels*), corrected for pitch angle motion in the limit of high mirror ratios ($q_\alpha = 2/\pi = 0.64$) and for helical twist by ≈ 1 radian ($q_H \approx 0.85$; Paper IV). The loop radius r is determined from the half-footpoint separation, corrected for the projection angle between the solar surface and line-of-sight direction. Finally, we determine for each flare the ratio l'/s, i.e., the TOF distance l' divided by the loop half length $s = r * (\pi/2)$.

Projections of the TOF distance l' into the vertical plane through the flare loop footpoints are shown in the left-hand panels in Figures 1, 2, 3, and 4, overlaid on HXT/M1 contours and SXT gray-scale images. In some exceptional cases, a missing SXT image was substituted by a HXT/Lo image, or the loop plane was tilted by an inclination angle θ so that the loop symmetry axis intersects with the cusp source (Figs. 1*a*, 1*b*, and 1*d*). The geometry is shown in projection onto the vertical plane in the second panels in Figures 1, 2, 3, and 4, containing the semicircular flare loop defined by the two footpoints, a magnetic field line that connects to the cusp with a length corresponding to the TOF distance l' (see definition in Paper VI). The start of the TOF distance l' is indicated by h_{ACC}, the supposed height of the acceleration site, and its uncertainty due to the Poisson noise of the HXR delay measurement is indicated with a thick error bar.

3.1. *Flares with Double Footpoint plus Coronal HXR Sources (Fig. 1)*

Figures 1*a*–1*e* contain five events with double footpoint sources plus an additional cusp source with $\gtrsim 30$ keV HXR emission (visible in the HXT/M1 channel). Three of these events (Figs. 1*b*, 1*c*, and 1*d*) are contained in Masuda's selection of 10 limb flares with above-looptop sources (Masuda 1994a). We found an additional limb flare (Fig. 1*e*), which occurred after the time range of Masuda's selection. This event of 1993 November 30 is special because it is the brightest SXR loop seen in SXT during the flare time overarches the coronal HXR source, but a difference image obtained from subtracting a preflare SXR image (shown as gray scale in Fig. 1*e*) reveals that a smaller new SXR loop grows underneath the coronal HXR source during the impulsive phase of the flare, while the overarching large loop remains stationary, probably a remnant postflare loop from a previous flare. We found also a cusp-shaped flare with a coronal HXR source on the disk (Fig. 1*a*, 1991 November 19), at a heliographic longitude of W64°, which otherwise resembles Masuda's limb flares with coronal above-looptop HXR sources.

The projections of the TOF distances onto the *Yohkoh*/HXT images show that the inferred acceleration site (defined by the start of a magnetic field line connecting with the footpoints) is cospatial with the location of the coronal HXR sources within the error bars of the HXR delay measurements for all five flares with coronal HXR sources. The first two flares (Figs. 1*a* and 1*b*) have relatively noisy HXR data and thus large error bars ($\sigma_{l'}/l' \approx 50\%$), but the other three flares have relatively small errors in the TOF distance

TABLE 2

GEOMETRIC PARAMETERS OF 52 ANALYZED FLARES

Date[a]	Start Time[b] (UT)	Duration[c] (s)	MER Channels[d]	MER Counts[e] (10^3 counts s^{-1})	HXT Counts[f] (counts s^{-1} SC^{-1})	Modulation Depth[g]	FFT Filter[h] t_F (s)	Spectral Slope γ[i]	Heliographic Position[j]	TOF Distance l'[k] (Mm)	Loop Radius r[l] (Mm)	Ratio l'/s[m]	Figure[n]	References
1) HXR Double Footpoints + Cusp Source														
911119.....	092825	50	1-3	22	17	0.17	7.0	4.83	S13W64	49.1 ± 28.6	9.6	3.27	1*a*	1
920113.....	172739	130	1-4	25	29	0.03	2.5	3.74	S16W85	41.6 ± 22.2	11.5	2.30	1*b*	2, 3
921004.....	221339	164	3-7	23	9	0.09	2.5	3.93	S08W85	19.6 ± 4.2	9.3	1.35	1*c*	2, 4
930217.....	103511	10	1-5	33	94	0.35	2.5	5.80	S06W89	33.6 ± 11.9	10.6	2.02	1*d*	2, 5
931130.....	060305	110	1-8	188	70	0.11	5.0	3.72	S20E83	24.3 ± 3.3	14.0	1.11	1*e*	
2) HXR Double Footpoints														
911031.....	090648	200	0-2	25	41	0.26	4.0	4.75	S13W37	17.4 ± 2.4	7.9	1.40	2*a*	
911109.....	205144	70	1-5	153	105	0.04	3.6	3.27	S14W69	16.0 ± 4.2	6.3	1.62	A1	6, 7
911110.....	200531	164	1-8	192	181	0.05	2.5	3.64	S11E47	20.0 ± 2.0	12.6	1.01	A2	6, 7, 8
911113.....	211555	130	1-7	115	52	0.12	2.5	3.80	S12E07	12.6 ± 1.3	6.9	1.16	2*b*	6
911115.....	223436	80	1-5	79	731	0.07	1.5	4.01	S14W18	26.8 ± 2.6	13.8	1.24	A3	6, 7, 9
911204.....	174302	164	1-7	116	70	0.10	2.0	4.08	N17E58	19.6 ± 2.8	11.9	1.05	A4	6, 7
911207.....	215155	120	2-4	17	17	0.19	3.5	4.98	N10E69	31.8 ± 7.7	17.7	1.15	2*c*	
911214.....	054837	40	1-5	63	32	0.15	1.5	4.78	N06W23	13.1 ± 2.3	5.3	1.58	2*d*	
911215.....	183220	65	3-9	199	157	0.19	3.0	2.76	S14E73	19.7 ± 1.3	6.8	1.84	A5	6, 7, 10
911216.....	010131	24	1-6	57	29	0.30	3.5	3.40	S27E02	9.1 ± 1.8	4.1	1.41	2*e*	
911216.....	044607	30	1-6	29	12	0.11	2.5	3.31	S11W45	28.3 ± 9.9	11.7	1.54	2*f*	6, 11
911216.....	131024	50	1-6	27	12	0.22	4.0	4.86	S10W40	17.0 ± 3.1	8.3	1.30	2*g*	
911226.....	213559	164	2-7	152	142	0.07	2.5	4.12	S14W18	31.0 ± 3.8	16.5	1.19	A6	6, 7
920203.....	004502	40	2-4	19	15	0.14	3.0	4.39	N31E36	18.7 ± 3.3	8.9	1.33	2*h*	
920207.....	034235	35	1-6	63	33	0.06	1.5	4.23	S16W47	15.6 ± 2.8	8.2	1.22	2*i*	12
920214.....	230649	100	5-9	141	918	0.09	1.8	3.33	S12E02	29.8 ± 7.7	11.7	1.63	A8	6, 7, 13
920625.....	175328	164	1-5	70	100	0.02	9.5	5.04	N10W75	58.5 ± 14.0	24.4	1.53	2*j*	6, 14
920805.....	212130	164	1-4	12	7	0.20	3.0	5.16	S13E31	18.4 ± 13.5	5.2	2.24	2*k*	
920906.....	090315	100	1-3	57	64	0.06	2.5	4.45	S08W35	17.2 ± 4.7	6.2	1.75	2*l*	15
921211.....	045829	40	1-4	12	5	0.33	2.0	4.46	S05W00	13.8 ± 3.9	7.9	1.28	2*m*	
930209.....	071840	100	1-5	31	20	0.15	2.0	4.83	S02E17	14.7 ± 8.3	5.5	1.71	2*n*	
931003.....	124231	30	2-4	30	19	0.16	3.0	3.82	N09W03	26.3 ± 8.0	14.7	1.14	2*o*	
3) HXR Single Footpoints, Elliptical														
911007.....	101710	16	1-5	11	7	0.16	3.5	3.80	N28W30	11.8 ± 8.0	4.3	1.74	3*a*	
911212.....	030023	60	1-4	42	27	0.15	3.0	4.58	S03E49	22.1 ± 3.2	9.9	1.42	3*b*	
911225.....	125415	164	1-6	82	54	0.11	3.0	4.37	S05E62	18.7 ± 2.8	8.8	1.35	3*c*	
911226.....	104801	124	1-7	166	89	0.12	1.0	3.77	N36W15	14.0 ± 2.0	5.9	1.52	A7	6, 7
920203.....	065826	25	1-4	39	22	0.22	1.0	4.86	S10E29	17.9 ± 2.9	7.5	1.53	3*d*	
920205.....	064317	26	1-5	40	17	0.23	1.5	3.97	S14W70	22.5 ± 6.0	10.3	1.40	3*e*	
920205.....	131601	80	1-6	75	46	0.12	3.5	4.81	S37W29	12.1 ± 1.9	6.0	1.27	3*f*	
920207.....	115117	90	2-5	22	47	0.11	2.0	4.27	S17W52	49.7 ± 12.1	14.7	2.16	3*g*	6, 16
930607.....	054214	130	1-5	26	16	0.22	2.5	4.42	S08W30	7.2 ± 3.4	4.0	1.14	3*h*	
931003.....	092457	66	1-6	82	40	0.08	2.5	4.01	N07W01	13.3 ± 3.7	7.5	1.13	3*i*	
940106.....	040531	38	1-6	45	24	0.24	1.0	3.68	S10W30	8.7 ± 2.0	3.7	1.50	3*j*	
940107.....	112714	70	1-5	46	2	0.21	3.5	4.78	S11W49	50.0 ± 3.2	14.7	2.17	3*k*	
940126.....	053954	25	2-8	103	59	0.19	2.5	2.90	N08W55	16.7 ± 2.4	7.1	1.51	3*l*	17
940814.....	173512	164	1-6	161	144	0.09	2.0	4.15	S11W06	18.4 ± 7.0	6.6	1.78	3*m*	

TABLE 2—*Continued*

Date[a]	Start Time[b] (UT)	Duration[c] (s)	MER Channels[d]	MER Counts[e] (10^3 counts s^{-1})	HXT Counts[f] (counts s^{-1} SC^{-1})	Modulation Depth[g]	FFT Filter[h] t_F (s)	Spectral Slope γ[i]	Heliographic Position[j]	TOF Distance l'[k] (Mm)	Loop Radius r[l] (Mm)	Ratio l'/s[m]	Figure[n]	References
4) HXR Single Footpoints, Unresolved														
920130.....	193708	164	1-4	20	21	0.15	3.0	5.05	S07W06	45.7 ± 19.2	...	...		
920624.....	185321	10	1-4	20	10	0.36	6.0	4.79	N10W56	18.7 ± 4.6	...	...		
920625.....	033409	25	1-6	55	23	0.30	2.5	3.37	N10W63	6.0 ± 1.8	<2.9	>1.32	4	
930514.....	220441	100	1-5	56	30	0.10	2.0	5.06	N19W48	9.7 ± 7.1	...	...		18
5) HXR Single Footpoints, near Limb														
911218.....	102652	70	1-5	93	106	0.06	3.0	5.58	S17E87	70.0 ± 6.7	...	...		
920811.....	222437	164	1-5	102	77	0.04	3.0	4.47	N15E80	31.3 ± 33.0	...	...		6
920907.....	184837	100	1-3	17	11	0.31	1.5	3.22	N14E82	8.6 ± 3.3	...	...		
921005.....	092428	120	1-6	34	18	0.20	4.0	4.26	S07W88	51.9 ± 27.0	...	...		
921012.....	215054	60	1-4	9	5	0.27	3.5	4.68	S19W88	31.0 ± 15.9	...	...		
930927.....	120730	164	1-5	56	41	0.04	2.5	4.66	N08E90	12.6 ± 8.9	...	...		
931112.....	180332	15	1-5	15	5	0.14	2.0	3.66	N11E78	41.5 ± 11.2	...	...		

[a] Observation date in YYMMDD.
[b] Start time of analyzed *CGRO/MER* time interval, in UT (HHMMSS).
[c] Duration of analyzed *CGRO/MER* time interval, in s.
[d] The range of *CGRO/MER* channels containing the HXR energy range over which TOF delays were measured, corresponding to the y-axis of the panels in the third column in Figs. 1, 2, 3, and 4. The MER channels have the following median energies ε_i for a HXR spectrum with a power-law slope of $\gamma = 4.0$: $\varepsilon_0 = 25$ keV, $\varepsilon_1 = 30$ keV, $\varepsilon_2 = 36$ keV, $\varepsilon_3 = 46$ keV, $\varepsilon_4 = 60$ keV, $\varepsilon_5 = 79$ keV, $\varepsilon_6 = 103$ keV, $\varepsilon_7 = 131$ keV, $\varepsilon_8 = 178$ keV, and $\varepsilon_9 = 250$ keV.
[e] *CGRO*/MER peak count rate measured in the analyzed time interval and summed over the analyzed energy channel range.
[f] Peak rate in the *Yohkoh*/HXT M1 channel recorded during the entire flare mode, in units of counts per second and subcollimator.
[g] The modulation depth or pulsed fraction is determined from the fluence ratio of the HXR pulses to the total HXR flux.
[h] The optimized FFT filter timescale t_F at which the TOF distance l' is measured.
[i] Slope of single power-law fit to HXR spectrum averaged over the analyzed time interval.
[j] Heliographic positions are measured for the midpoint of the flare loops.
[k] Electron time-of-flight distance l', corrected for pitch angle and helical twist, i.e. $l' = l * q_\alpha q_H = l * 0.54$.
[l] Loop radius r or half footpoint separation.
[m] Ratio of time-of-flight distance l' to loop half-length $s = r * (\pi/2)$.
[n] Figure labels in this paper (Figs. 1*a*–1*e*, 2*a*–2*o*, 3*a*–3*n*) and to Paper VI (labels A1–A8).

REFERENCES.—(1) Culhane et al. 1992; (2) Masuda 1994a; (3) Masuda et al. 1994, Masuda et al. 1995, Takakura et al. 1993, Doschek 1994, Kosugi 1994, Doschek, Strong, & Tsuneta 1995, Wang et al. 1995a, Hudson 1994, Hudson & Ryan 1995, Wheatland & Melrose 1995, Shibata et al. 1995, Paper IV; (4) Masuda 1994b, Masuda et al. 1995; (5) Masuda et al. 1995; (6) Sakao 1994; (7) Paper VI; (8) Yoshimori et al. 1992, Inda-Koide et al. 1995; (9) Sakao et al. 1992, Hudson et al. 1992, Canfield et al. 1992, Kane et al. 1993b, Kane et al. 1993a, McTiernan et al. 1994, Kawabata et al. 1994a, Kawabata et al. 1994b, Culhane et al. 1993, Wuelser et al. 1994, Inda-Koide et al. 1995; (10) Paper V; (11) Culhane et al. 1994a, Culhane et al. 1994b, Sakao et al. 1994, Inda-Koide et al. 1995; (12) Feldman et al. 1994; (13) Hudson et al. 1994; (14) Anwar et al. 1994; Hanaoka 1994, Wang et al. 1995b; (15) Yaji et al. 1994, Zarro et al. 1994, Kato & Fujiwara 1994; (16) Sakao et al. 1994; (17) Takano & Nishio 1995; (18) Nakajima et al. 1994.

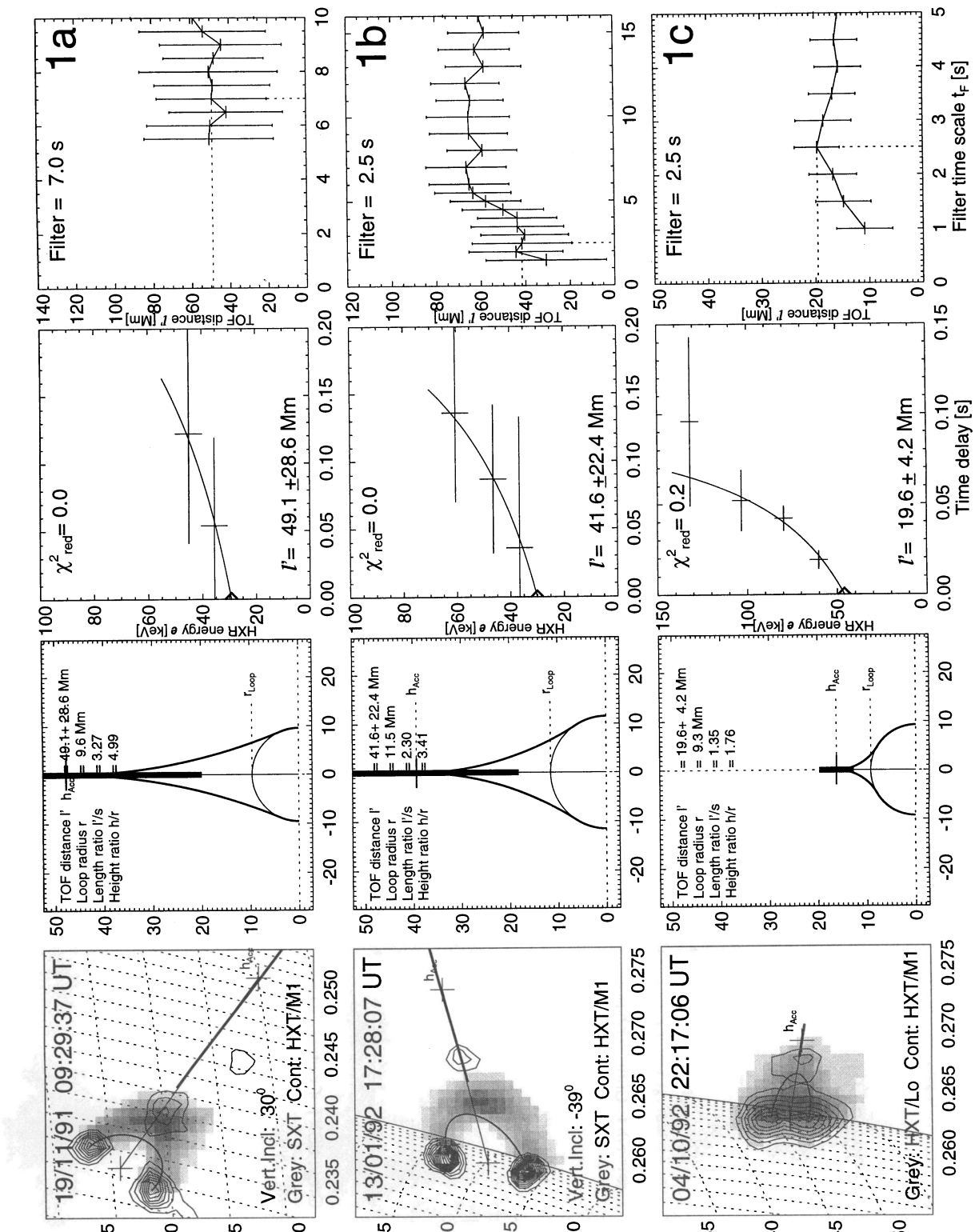

FIG. 1.—Five events with HXR double footpoints and cusp sources. The left panels show overlays of HXT and SXT images (grayscale images and contours are identified at the bottom of the panels in the left-hand column). The heliographic grid has always a spacing of 1° (= 12,500 km). The loop geometry is indicated with a semicircle, the vertical symmetry axis with a thin line, and the error bars of the start of the time-of-flight (TOF) distance with thick error bars. The loop plane is almost always vertical to the solar surface, except when an inclination angle is given (bottom of panels on left-hand side). A representation of the vertical plane is shown in the panels of the second column. The third column shows the fit of the TOF model to the measured HXR delays. The fourth column shows the TOF distance as function of the FFT filter timescale, with the optimized value indicated with dashed lines.

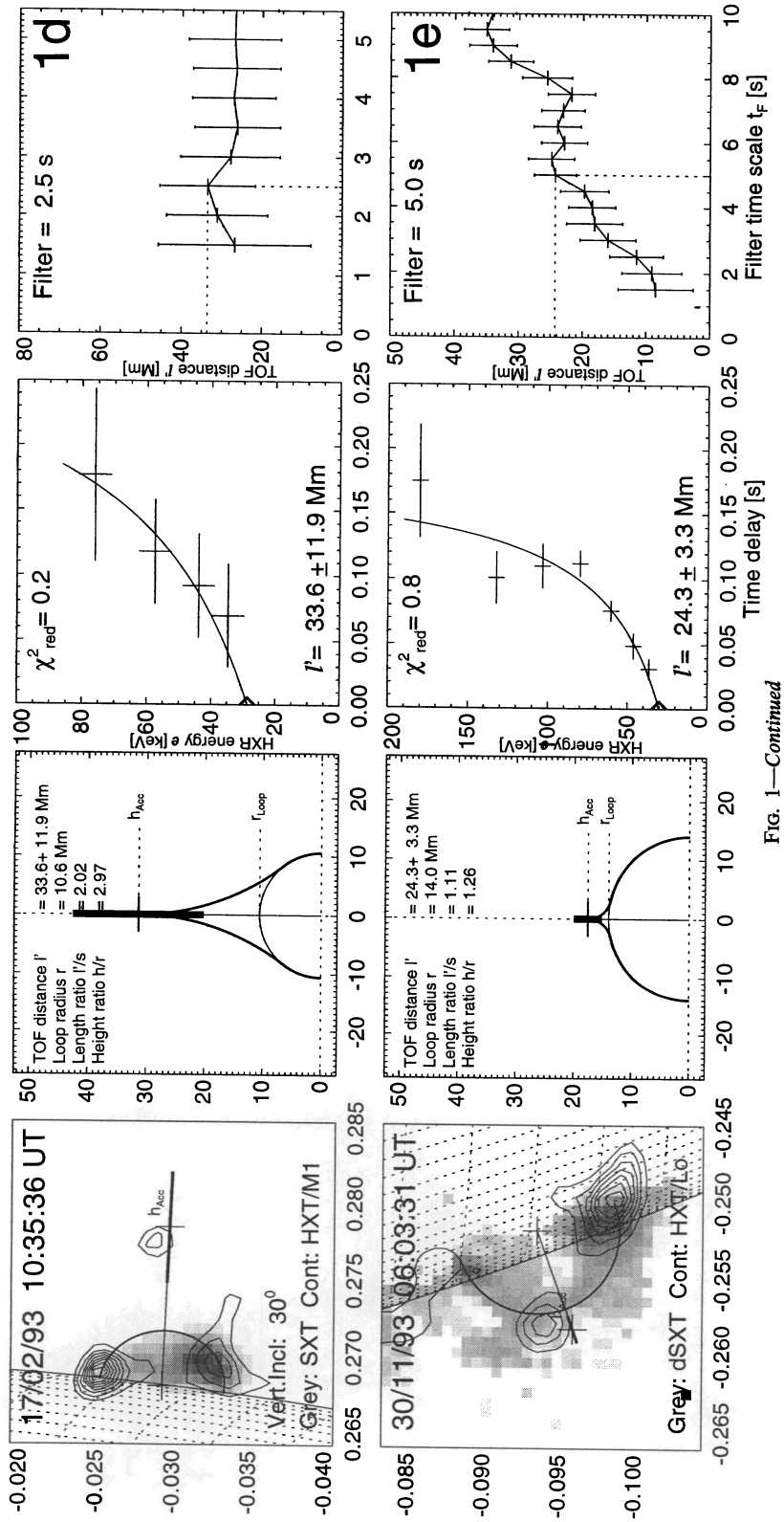

FIG. 1—*Continued*

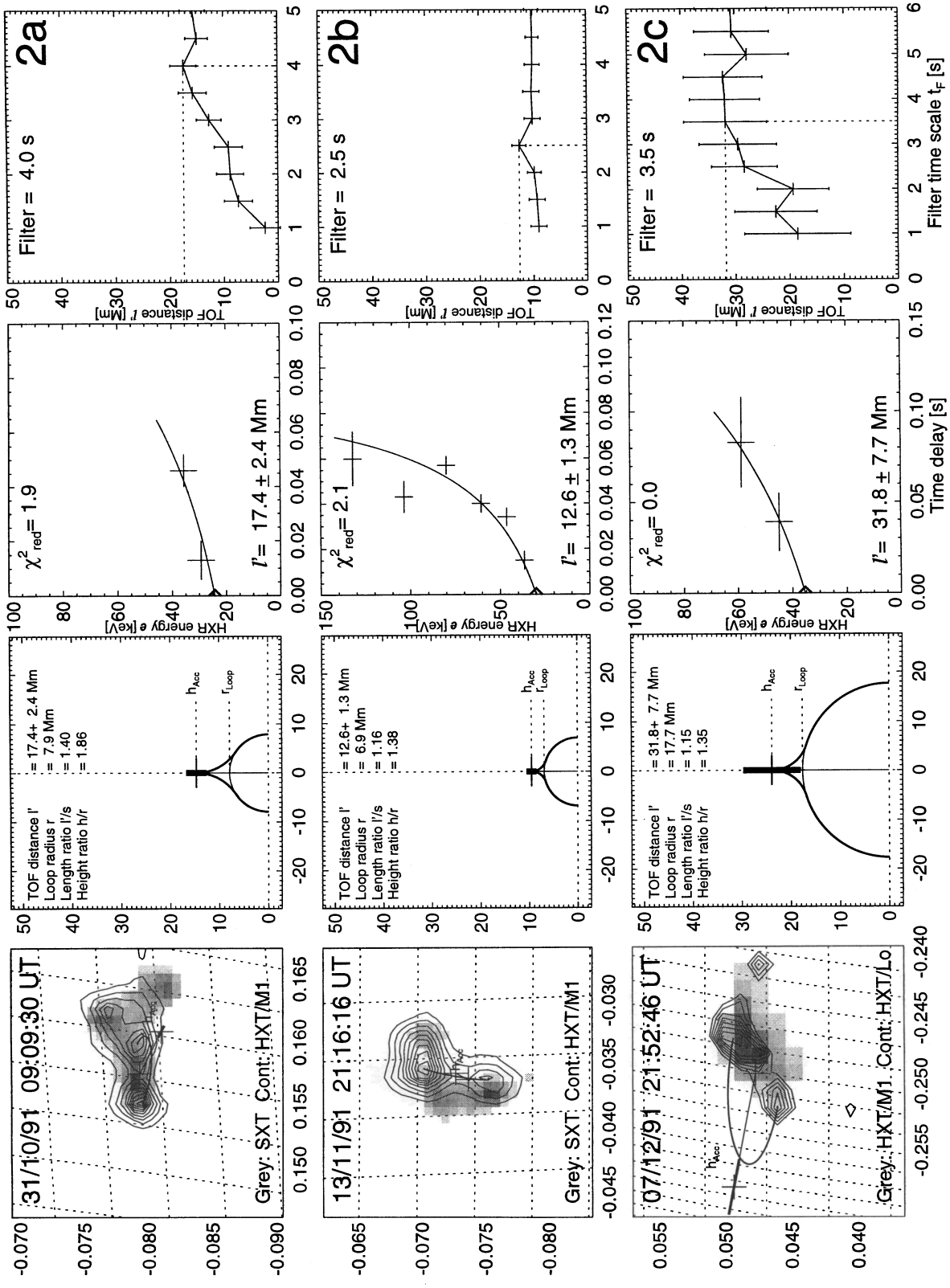

FIG. 2.—Fifteen events with resolved HXR double footpoint sources. Representation similar to Fig.1.

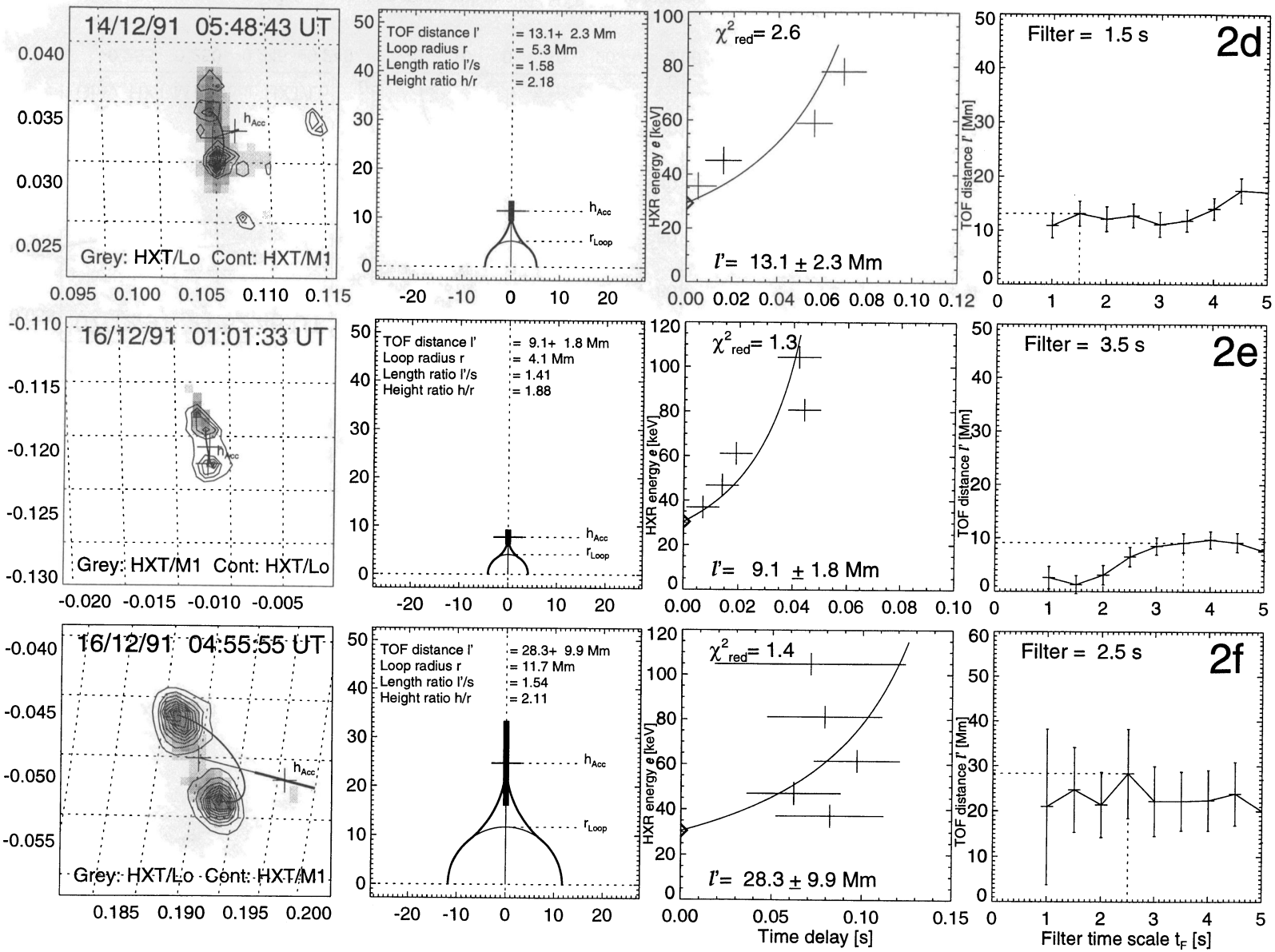

FIG. 2—*Continued*

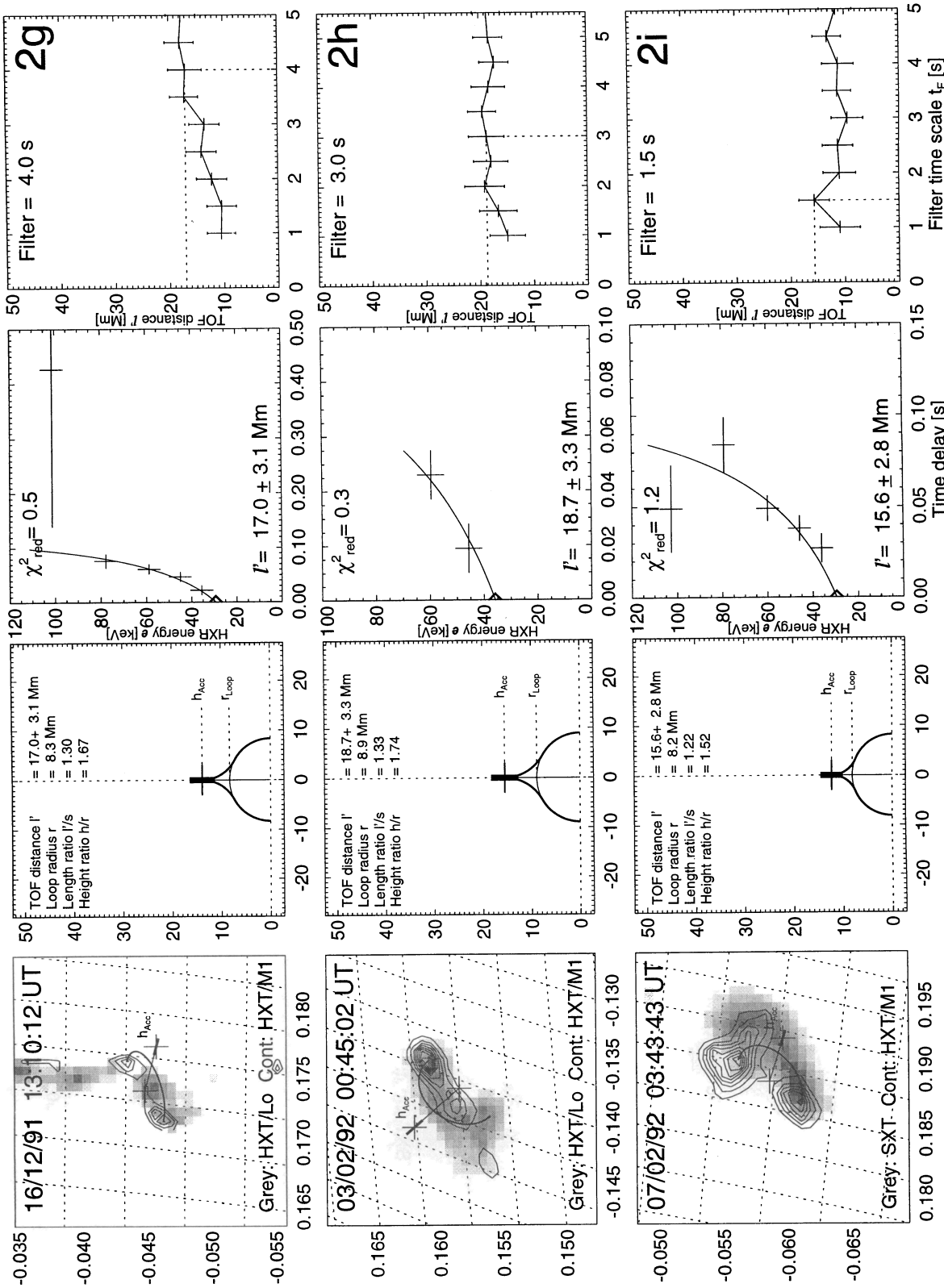

FIG. 2—*Continued*

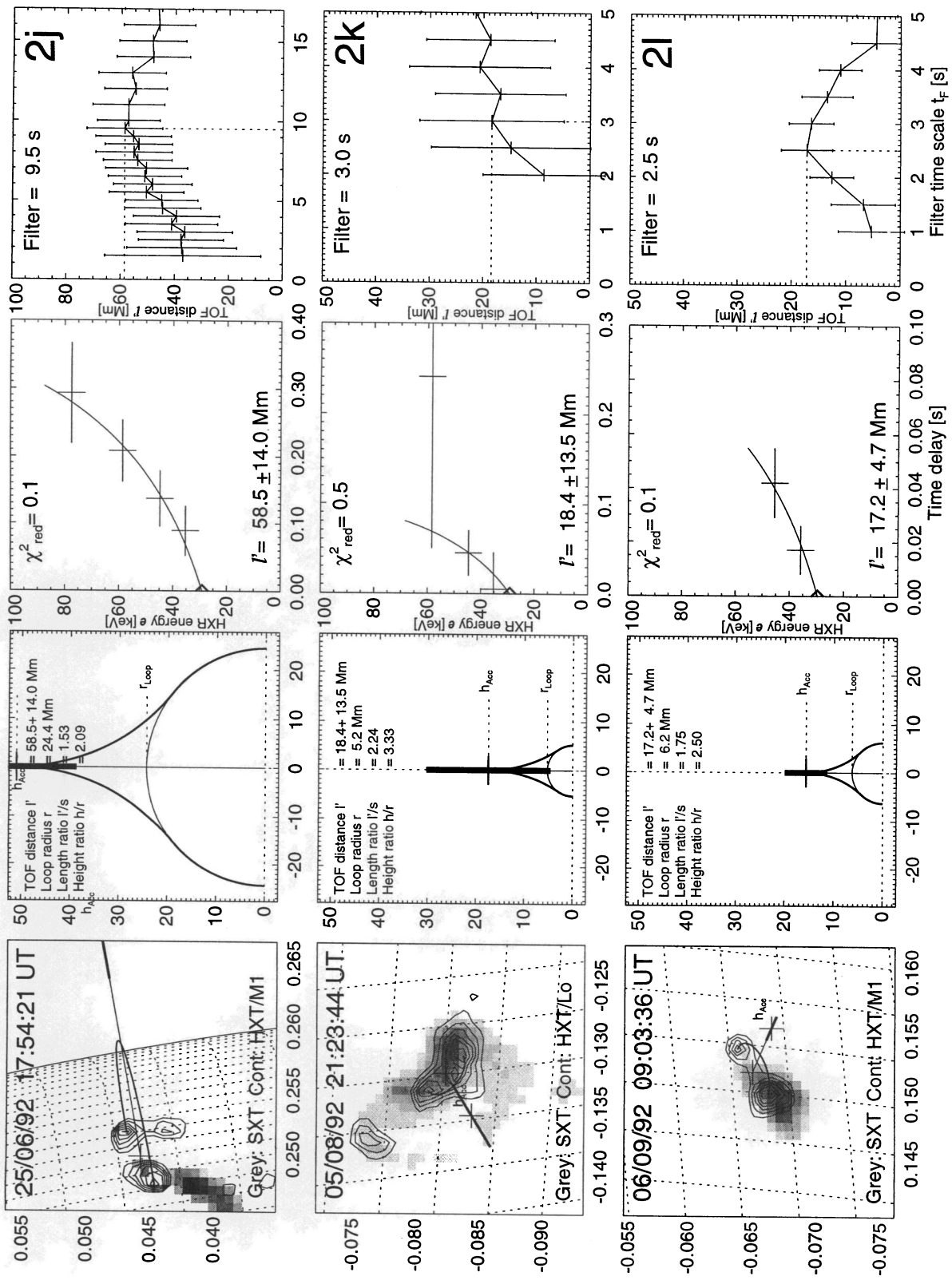

FIG. 2—*Continued*

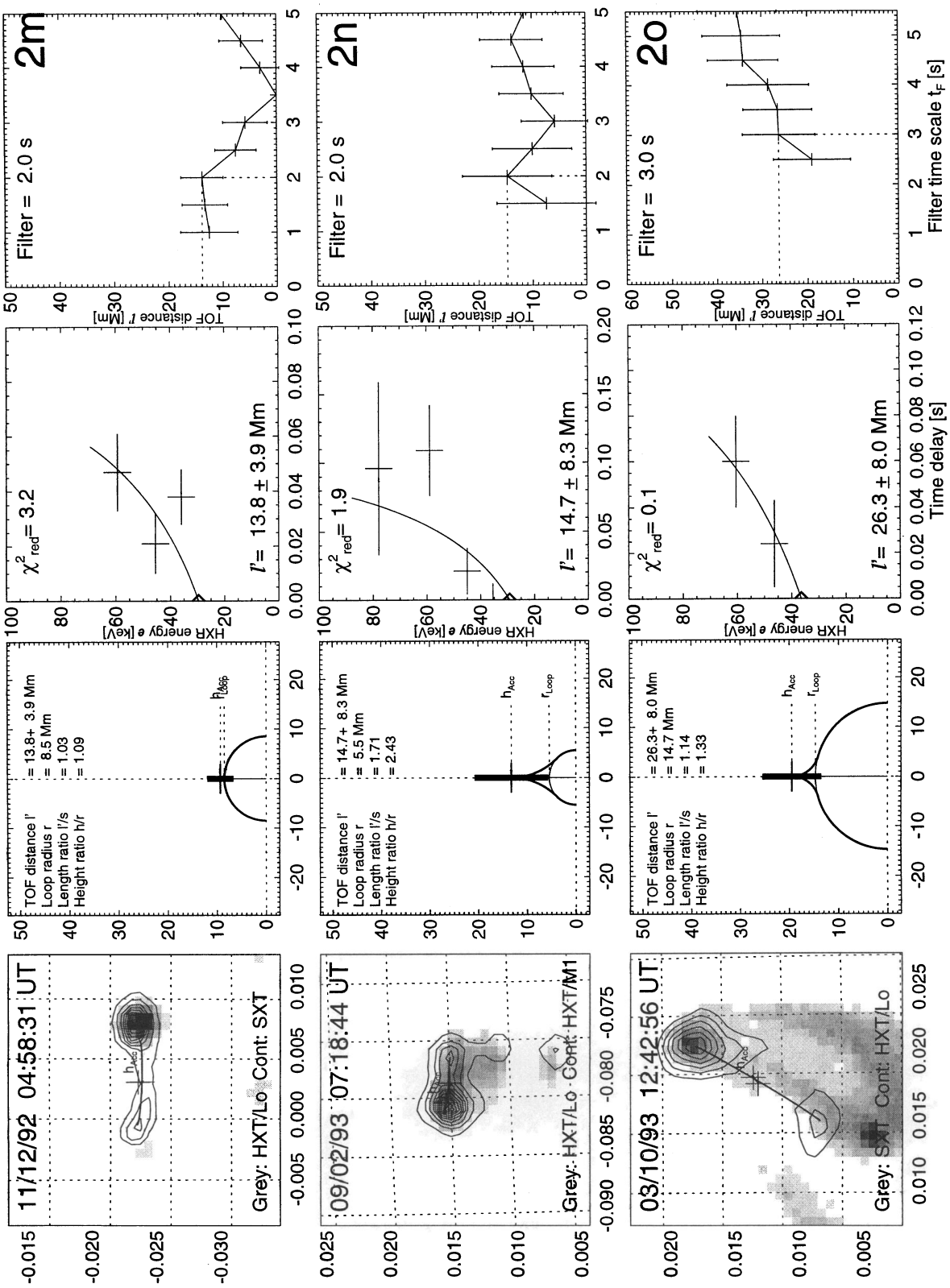

FIG. 2—*Continued*

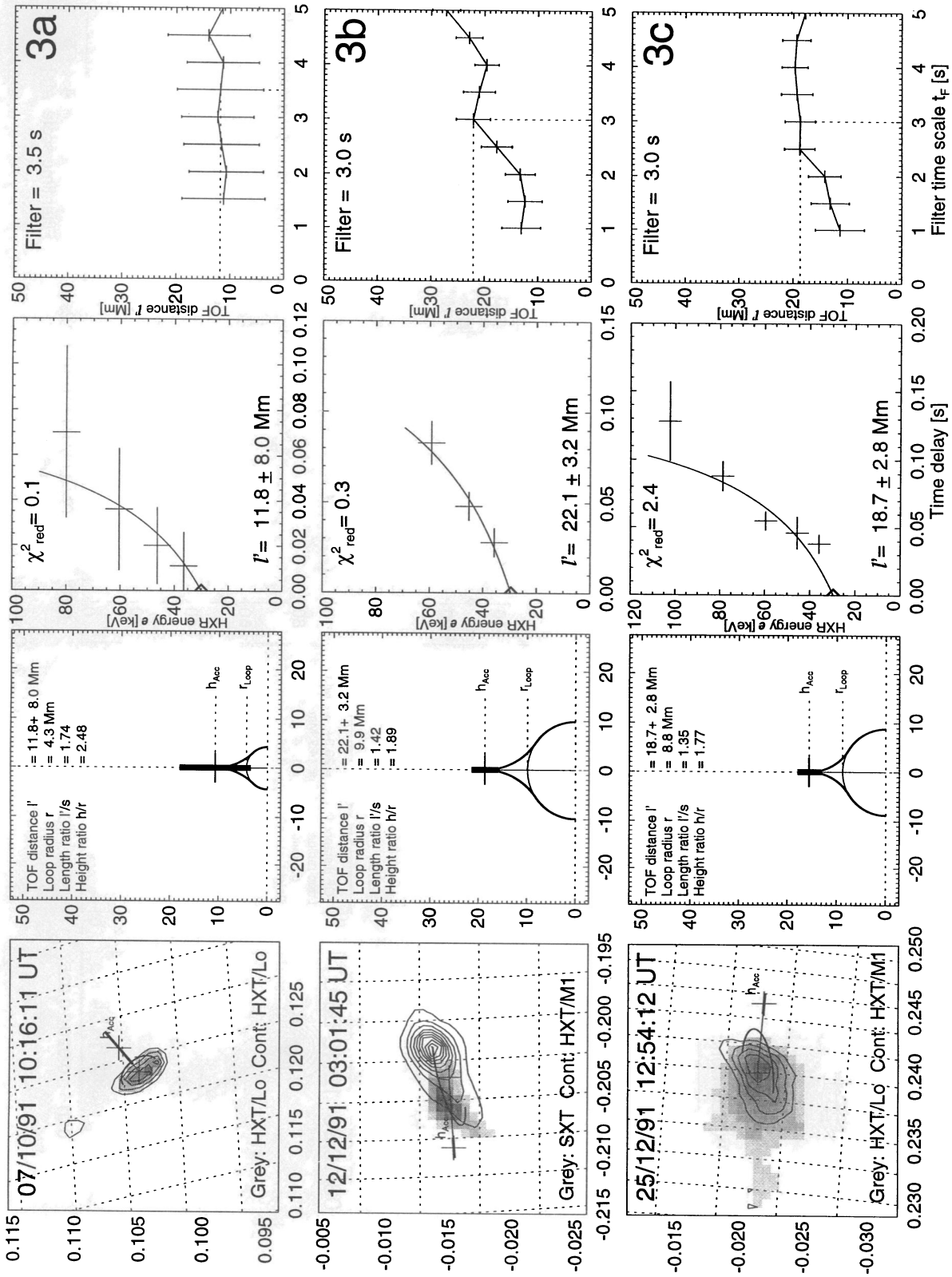

FIG. 3.—Thirteen events with unresolved HXR double footpoint sources. Representation similar to Fig.1.

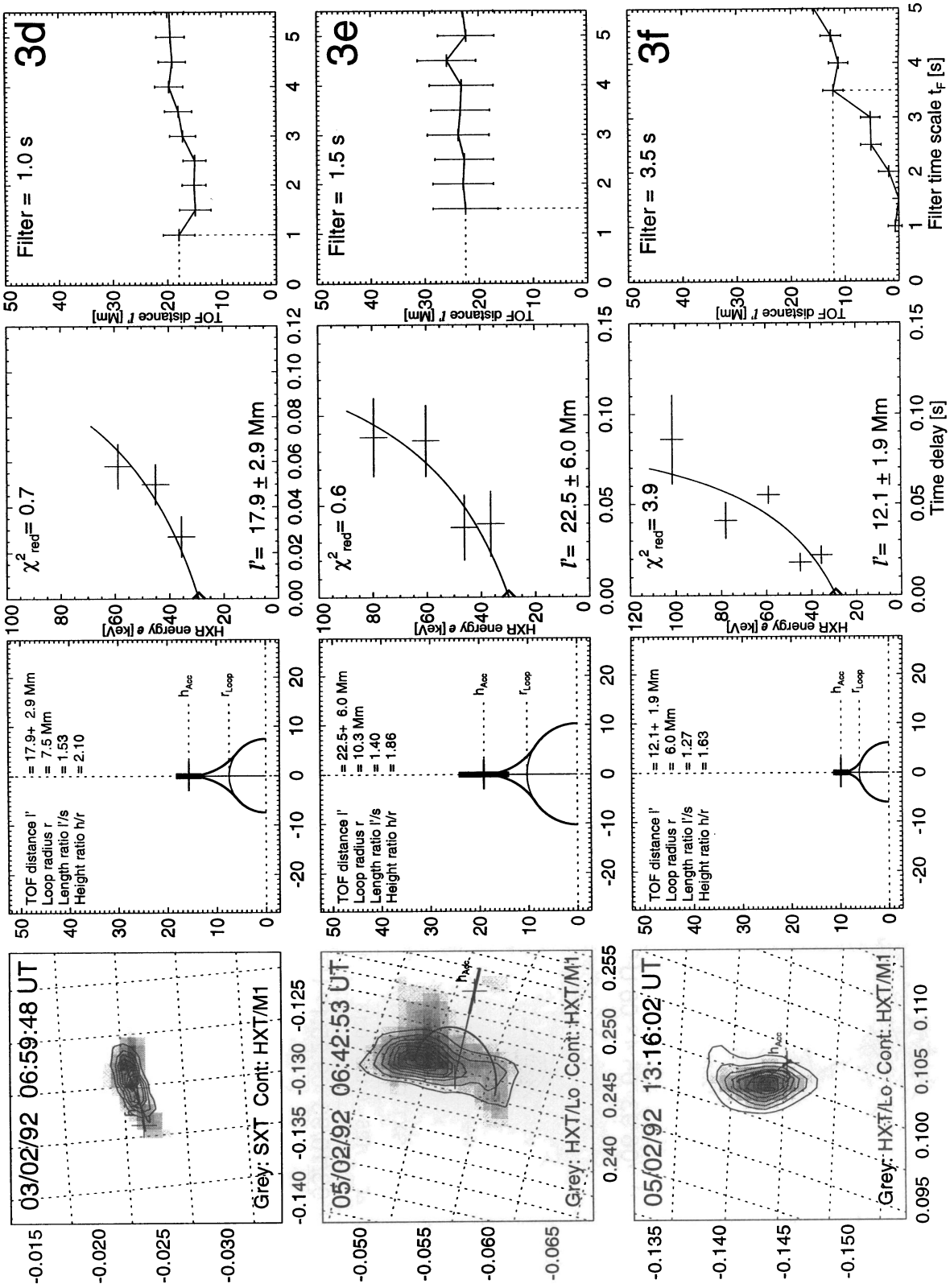

FIG. 3—*Continued*

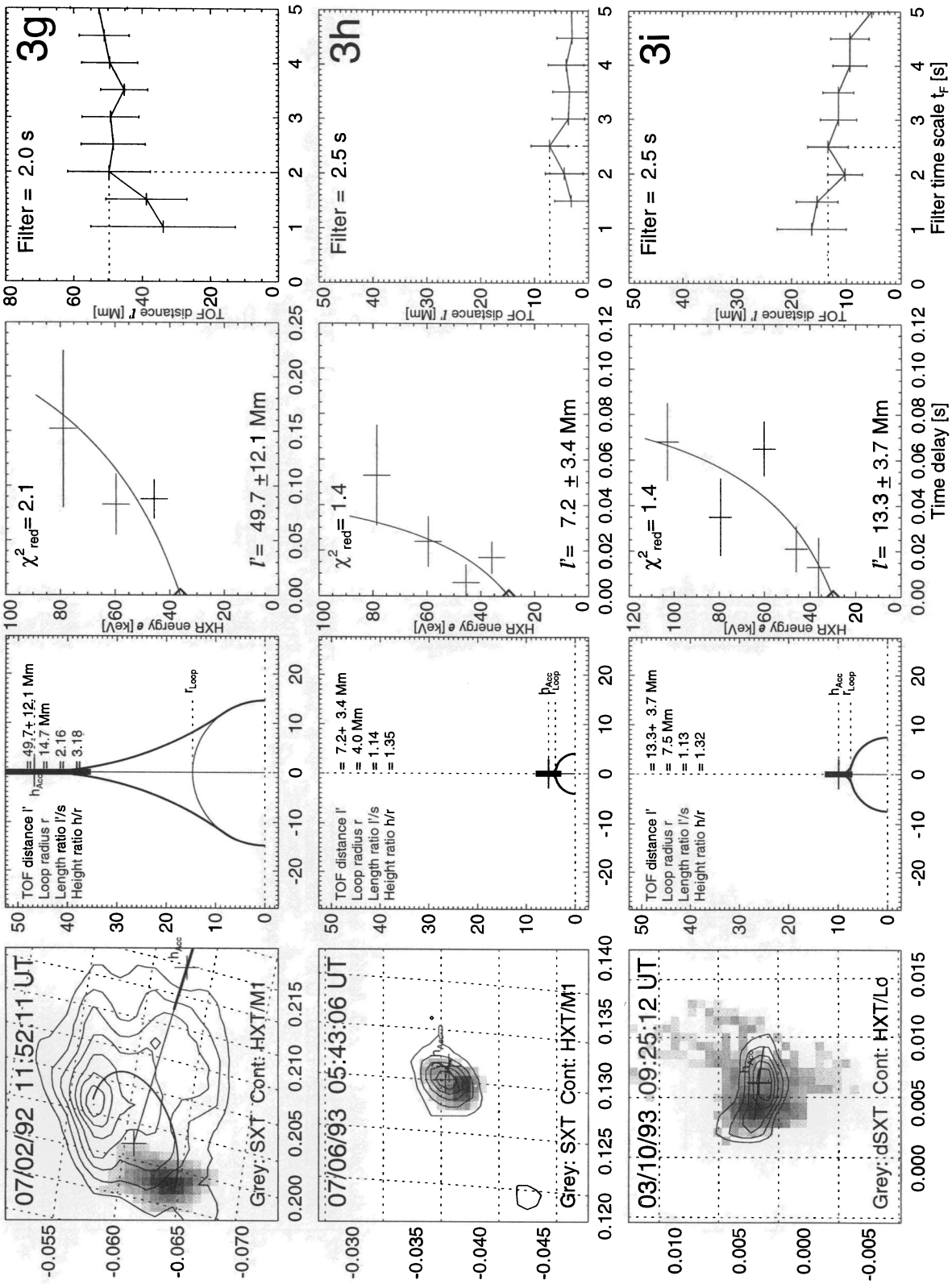

FIG. 3—*Continued*

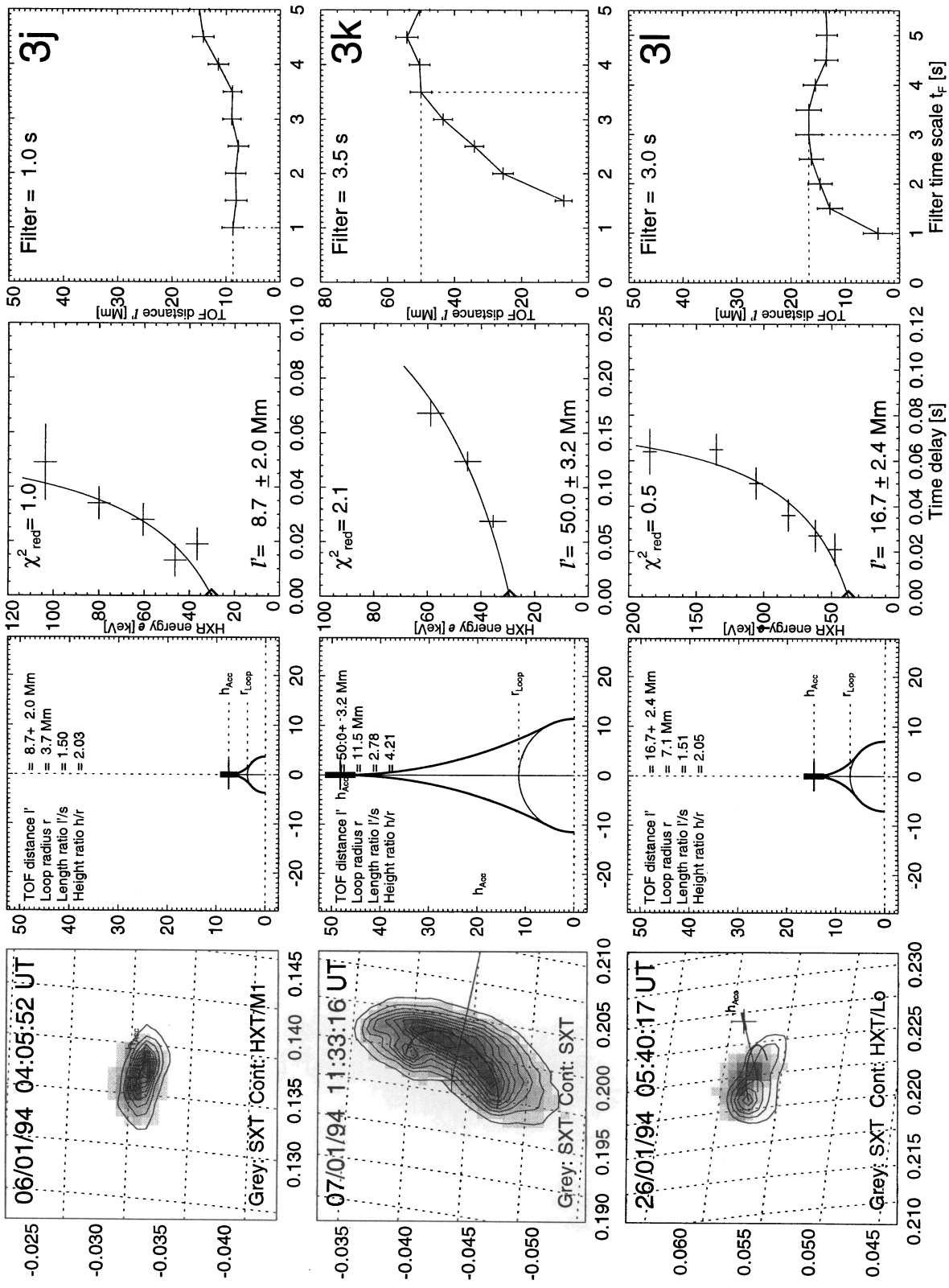

FIG. 3—*Continued*

1996ApJ...470.1198A

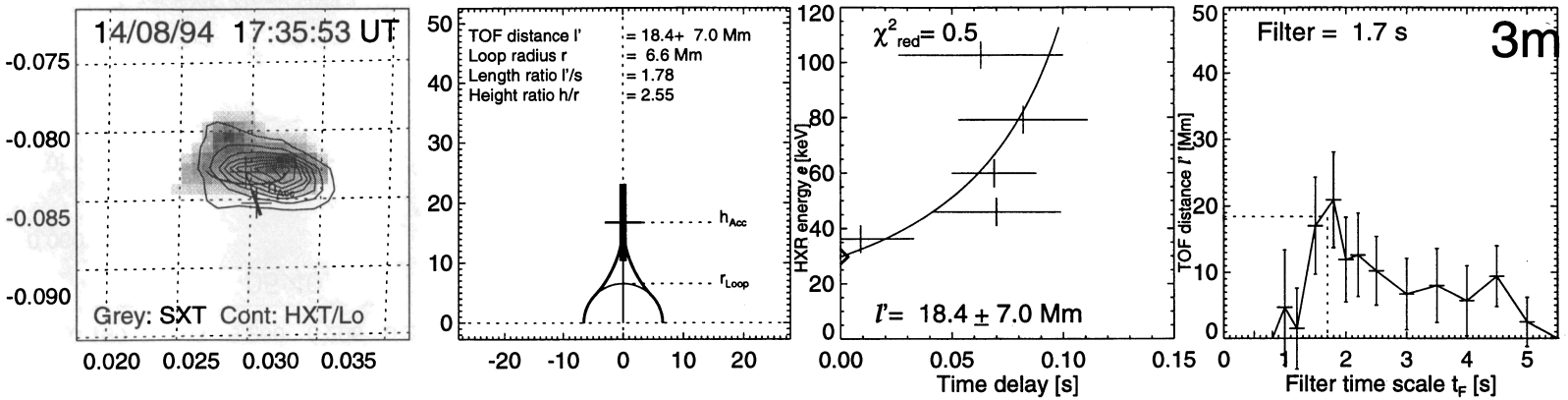

FIG. 3—*Continued*

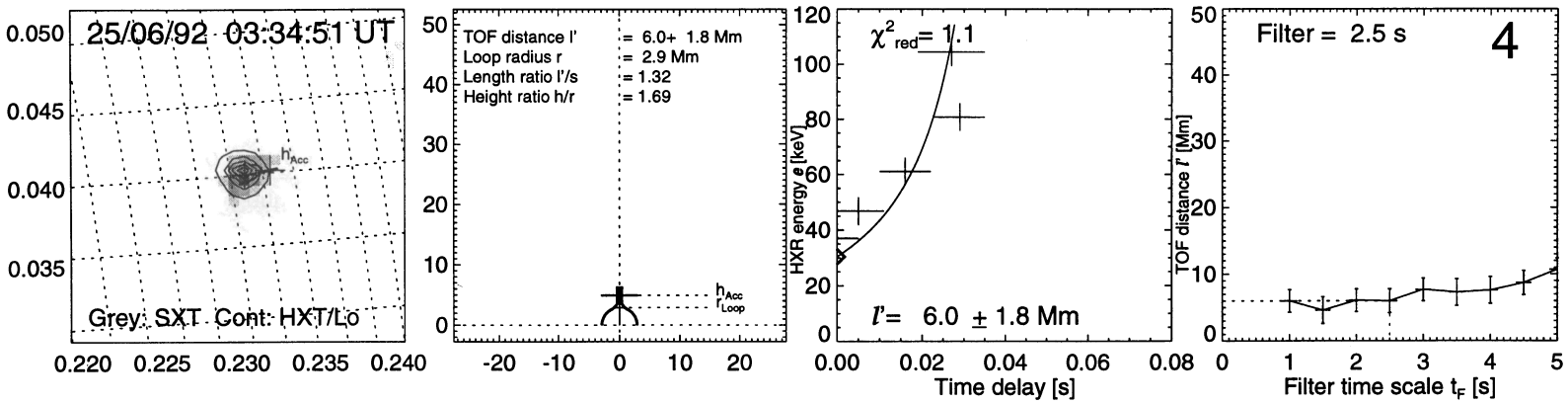

FIG. 4.—One event with HXR single footpoint source. Representation similar to Fig.1.

($\sigma_{l'}/l' \approx 15\%$–$35\%$) and match the location of the coronal HXR sources quite closely. The flare of 1992 January 13 has been previously investigated in Paper IV. Although we used different filter techniques to separate the HXR pulses from the smooth HXR flux in the two studies, we find a consistent TOF distance with both techniques.

3.2. *Flares with Resolved HXR Double Footpoint Sources (Fig. 2)*

The second group contains classical double footpoint flares, as studied by Hoyng et al. (1981), Duijveman, Hoyng, & Machado (1982), Takakura et al. (1984), and Sakao (1994). From this group of 22 flares, the seven largest flares are shown in Paper VI, while the 15 weaker flares are shown here in Figure 2. Only few flares have symmetric footpoints (e.g., Fig. 2*f*); most of them have an asymmetric HXR brightness in both footpoints, probably caused by asymmetric magnetic mirror ratios (Sakao 1994). The contemporaneous SXT image does not always show a SXR loop connecting the two footpoints. Such discrepancies can be explained by the presence of preexisting bright SXR loops, while the upflow of SXR-emitting plasma from the conjugate HXR footpoints could be delayed or weaker compared with the preexisting SXR loop. In some cases, the contours of the flare-related SXR loops were used to identify the conjugate footpoints (e.g., Fig. 2*m*).

3.3. *Flares with Unresolved HXR Double Footpoint Sources (Fig. 3)*

This group of 14 flares, shown in Figure 3, has an intermediate morphology between double and single footpoint sources. We interpret most of these cases as a superposition of two (mostly asymmetric) double footpoint sources, which cannot be properly resolved in the HXT images, either because of the spatial proximity and asymmetry or because of confusion by additional HXR contributions from coronal parts of the flare loop. To estimate the (unresolved) footpoint separation, we use the elliptical shape of the lower brightness contours as a guide. However, because this determination of footpoint separation is less certain, we sample the statistics of loop geometries separately for this group.

3.4. *Flares with HXR Single Footpoint Sources (Fig. 4)*

There remain 11 flares with single footpoint sources for which the footpoint separation cannot be determined. One case is shown in Figure 4, for which the TOF distance is comparable with the spatial resolution of HXT, so that we suspect that the two footpoints cannot be resolved. In three other flares, listed under Group 4 in Table 2, the TOF distance is definitely larger than the resolution of HXT, so that we suspect that the conjugate HXR footpoint is too weak to be visible in the HXT images, given the maximum HXT dynamic range of $\approx 1{:}10$ and the relatively weak HXT count rates for these events. A last group of seven flares with single sources is located near the limb, for which we suspect that the double footpoint structure cannot be resolved because of the foreshortening in the east-west direction.

3.5. *Scaling Law between Electron TOF Distances and Loop Lengths*

After removing flares with single sources, for which the footpoint separation cannot be determined, we are left with

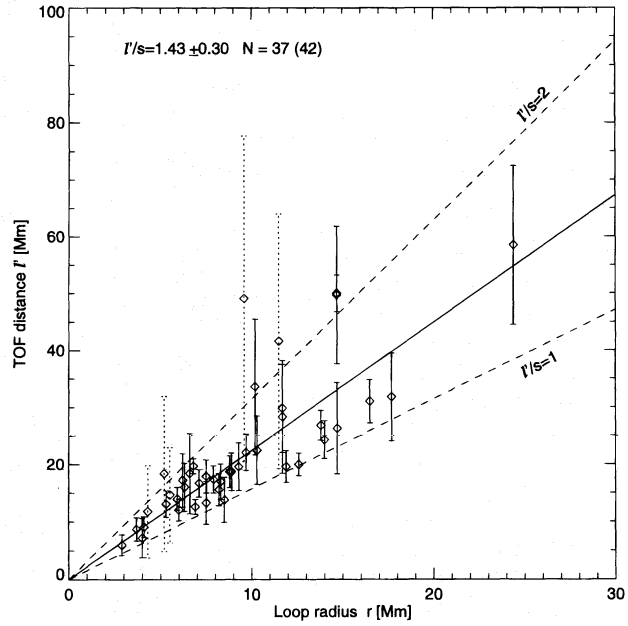

FIG. 5.—Scaling law of TOF distance l' vs. loop radius r in 42 flare events. The average ratio is indicated with a solid line; the dashed lines indicate a loop half-length ($l'/s = 1$) or a full loop length ($l'/s = 2$).

42 events for which both the TOF distance and the footpoint separation is known. For these 42 events, we plot the TOF distance l' versus the loop radius r in Figure 5. The loop radii vary from a maximum of $r = 25{,}000$ km down to the HXT resolution limit of $r \approx 3000$ km. There is a striking correlation between the two parameters. We find a mean ratio of $l'/s = 1.43 \pm 0.30$ for the TOF distance l' to the loop half-length $s = r * (\pi/2)$, omitting events with large uncertainties in the TOF distance, i.e., five events with $\sigma_{l'}/l' \gtrsim 50\%$ (indicated with dashed error bars in Fig. 5). For the subset of elongated (elliptical) HXR sources, we find no significant difference in the ratio l'/s. All ratios are confined in a range of $1 \leq l'/s \lesssim 2$, although the range of loop radii varies by a factor of 10. We do not find a single flare with a TOF distance shorter than the loop half-length. All flares with ratios $l'/s > 2$ have also large error bars and could be consistent with a ratio of $l'/s < 2$. The completeness of this data set (that includes all flares with measurable footpoint separation and HXR pulse delays of positive sign) constitutes a highly representative result, which may be dubbed the "*scaling law*" *between the electron TOF distance and flare loop length.*

4. DISCUSSION AND CONCLUSIONS

The main result of this study is a scale-invariant ratio between the electron TOF distance l' and the flare loop half-length s, i.e., $l'/s = 1.4 \pm 0.3$. Because this ratio is smaller than 2, the acceleration site of electrons that produce footpoint HXR emission could theoretically be located inside the flare loop. However, there are two independent reasons that support evidence for a location of the acceleration site *above* the flare loop rather than in the loop itself.

The most direct reason is the presence of HXR sources above the flare looptop, as identified by Masuda (1994a) and shown in the five cases in Figure 1 here. Moreover, we found that the electron TOF distance matches the separa-

tion between the coronal HXR sources and the footpoints. This probably represents the strongest evidence to identify the coronal HXR sources with the electron acceleration site, although the physics of nonthermal HXR emission in such low-density regions is poorly understood (Hudson & Ryan 1995). A possible explanation is that trapping is involved in the acceleration region, which bottles up the electrons until they get injected (or scattered) into the flare loop. Because the timescale of the modulated pulses appears to be correlated with the loop diameter (see Fig. 9 in Paper VI), the injection mechanism could be a pitch-angle modulation mechanism controlled by MHD oscillations or MHD waves in the cusp region. This scenario would also explain the apparent simultaneity of the electron injection times at different energies.

A second reason in favor of an acceleration site outside of the flare loop is the fact that the average ratio l'/s deviates from unity. To understand this, we have to be aware that the HXR pulses with a typical duration of ≈ 0.5–1.5 s (Paper VI) are much longer than the measured electron propagation time differences (of ≈ 0.1 s) and therefore do not allow us to measure the propagation times to the two footpoints separately. For instance, if we assume that an acceleration site is located 1.4 loop half-lengths away from one footpoint, and thus 0.6 half-lengths away from the other footpoint, the superimposed HXR pulses from both footpoints would add up to a single pulse with a TOF difference that corresponds approximately to the mean delay from both contributions, i.e., corresponding to 1.0 loop half-lengths, unless the contributions from both footpoints are so asymmetric that the contribution from one footpoint dominates in the delay measurement. However, inspecting the most symmetric footpoint sources (e.g., cases shown in Figs. 2*f* or 2*j*), we find the same nonunity ratios of $l'/s \approx 1.5$ as for the asymmetric loops.

In view of these arguments, it appears that electron acceleration is most likely to be located in the cusp region above the flare loops. It remains to be shown whether the acceleration site is located in the immediate environment of an X-type magnetic reconnection point or in some region below, e.g., in a region of turbulent outflow from the reconnection point (LaRosa et al. 1996; Moore, La Rosa, & Orwig 1995; Tsuneta 1996). Once the accelerated electrons get injected into the flare loop, only the fraction with small pitch angles will directly precipitate at one or at both footpoints, depending on the local magnetic mirror ratios. In large loops with high magnetic mirror ratios, we expect that all injected electrons are bounced first before they scatter into a loss cone and precipitate, producing a smoother HXR time profile without fast time structures and exhibiting delays that are characteristic of the trapping times. This scenario explains, in a natural way, the generally small modulation depth ($\lesssim 5\%$–20%) of the HXR pulses and why the time delays of the modulated HXR pulses are consistent with electron time-of-flight differences, while the smooth HXR flux is governed by opposite time delays characteristic of electron trapping times. We should not forget that this scenario applies for flares with HXR footpoint emission. If the electron density in the flare loop is sufficiently high ($n_e \gtrsim 10^{12}$ cm^{-3}), electrons will lose a significant fraction of their energy by Coulomb collisions in the coronal part of the flare loop. We will investigate this class of flares with dominantly coronal HXR emission in a separate study.

The *Yohkoh* data used in this paper were provided by the *Yohkoh* mission of ISAS, Japan, which was prepared and is operated by the international collaboration of Japanese, US, and UK scientists under the support of ISAS, NASA, and SERC, respectively. We are grateful to Taro Sakao and Jim McTiernan for developing the HXT-MULTIMG interface. We thank Nariaki Nitta and David Alexander for showing us comparisons with pixon maps of HXT images. The *CGRO* data were obtained through the Compton Observatory Science Support Center GOF account, provided by GROSSC and the BATSE Team. We thank the BATSE P.I. team G. Fishman, W. Paciesas, G. Pendleton, R. Wilson, C. Meegan, and R. Preece at MSFC, T. McGlynn at the *CGRO* science support center (GROSSC). The Solar Data Analysis Center at GSFC managed by J. Gurman is acknowledged for providing computational and database facilities. The work of M. J. A. was supported by SR&T grant NAG-5-2352, the work of H. S. H. by NASA grant NAS-8-37334, the work of R. A. S. by CGRO grant NAS-5-32584, and the work of M. J. W. by NASA cooperative agreement NCC 5-83 and NSF grant ATM-9400746.

REFERENCES

Anwar, B., Hiei, E., Hudson, H. S., Acton, L. W., Lemen, J., & Metcalf, T. R. 1994, in New Look at the Sun with Emphasis on Advanced Observations of Coronal Dynamics and Flares, ed. S. Enome & T. Hirayama (Nobeyama Report 360), 137
Aschwanden, M. J. 1996, in AIP Conf. Proc. 374, High Energy Solar Physics, ed. R. Ramaty, N. Mandzhavidze, & X.-M. Hua (New York: AIP), 300 (Paper V)
Aschwanden, M. J., Hudson, H., Kosugi, T., & Schwartz, R. A. 1996a, ApJ, 464, 985 (Paper IV)
Aschwanden, M. J., Montello, M. L., Dennis, B. R., & Benz, A. O. 1995a, ApJ, 440, 394
Aschwanden, M. J., & Schwartz, R. A. 1995, ApJ, 455, 799 (Paper II)
———. 1996, ApJ, 464, 974 (Paper III)
Aschwanden, M. J., Schwartz, R. A., & Alt, D. M. 1995b, ApJ, 447, 923 (Paper I)
Aschwanden, M. J., Wills, M. J., Hudson, H. S., Kosugi, T., & Schwartz, R. A. 1996b, ApJ, 468, 398 (Paper VI)
Brown, J. C. 1971, Sol. Phys., 18, 489
Canfield, R. C., et al. 1992, PASJ, 44, L111
Culhane, J. L., et al. 1992, PASJ, 44, L101
Culhane, J. L., et al. 1993, Adv. Space Res., 13(9), 303
Culhane, J. L., et al. 1994a, Sol. Phys., 153, 307
Culhane, J. L., Phillips, A. T., Kosugi, T., Inda-Koide, M., & Pike, C. D. 1994b, in New Look at the Sun with Emphasis on Advanced Observations of Coronal Dynamics and Flares, ed. S. Enome & T. Hirayama (Nobeyama Report 360), 117
Doschek, G. A. 1994, in New Look at the Sun with Emphasis on Advanced Observations of Coronal Dynamics and Flares, ed. S. Enome & T. Hirayama (Nobeyama Report 360), 173
Doschek, G. A., Strong, K. T., & Tsuneta, S. 1995, ApJ, 440, 370
Duijveman, A., Hoyng, P., & Machado, M. E. 1982, Sol. Phys., 81, 137
Emslie, A. G. 1978, ApJ, 224, 241
———. 1983, ApJ, 271, 367
Feldman, U., Hiei, E., Phillips, K. J. H., Brown, C. M., & Lang, J. 1994, ApJ, 421, 843
Fishman, G. J., et al. 1989, in The Burst and Transient Source Experiment (BATSE)—Scientific Objectives and Capabilities, Proc. GRO Science Workshop, ed. W. N. Johnson (Greenbelt: GSFC), 2-39
Fishman, G. J., Meegan, C. A., Wilson, R. B., Paciesas, W. S., & Pendleton, G. N. 1992, in The Compton Observatory Science Workshop (NASA CP 3137), ed. C. R. Shrader, N. Gehrels, & B. R. Dennis (Greenbelt: GSFC), 26
Hanaoka, Y. 1994, in New Look at the Sun with Emphasis on Advanced Observations of Coronal Dynamics and Flares, ed. S. Enome & T. Hirayama (Nobeyama Report 360), 181
Holman, G. D. 1985, ApJ, 293, 584
Hoyng, P., et al. 1981, ApJ, 244, L153
Hudson, H. S. 1972, Sol. Phys., 24, 414

Hudson, H. S. 1994, in High-Energy Solar Phenomena—A New Era of Spacecraft Measurements, ed. J. M. Ryan & W. T. Vestrand (New York: AIP), 151
Hudson, H. S., Acton, L. W., Hirayama, T., & Uchida, Y. 1992, PASJ, 44, L77
Hudson, H. S., & Ryan, J. 1995, ARA&A, 33, 239
Hudson, H. S., van Driel-Gesztelyi, L., & Kosugi, T. 1994, in New Look at the Sun with Emphasis on Advanced Observations of Coronal Dynamics and Flares, ed. S. Enome & T. Hirayama (Nobeyama Report 360), 397
Inda-Koide, M., Makishima, K., Kosugi, T., & Kaneda, H. 1995, PASJ, 47, 661
Kane, S. R., Hurley, K., McTiernan, J. M., & Sommer, M. 1993a, Adv. Space Res., 13(9), 241
Kane, S. R., McTiernan, J. M., Loran, J., Lemen, J., Yoshimori, M., Ohki, K., & Kosugi, T. 1993b, Adv. Space Res., 13(9), 237
Kato, T., & Fujiwara, T. 1994, in New Look at the Sun with Emphasis on Advanced Observations of Coronal Dynamics and Flares, ed. S. Enome & T. Hirayama (Nobeyama Report 360), 191
Kawabata, K., Yoshimori, M., Suga, K., Morimoto, K., Hiraoka, T., Sato, J., & Ohki, K. 1994a, ApJS, 90, 701
———. 1994b, in New Look at the Sun with Emphasis on Advanced Observations of Coronal Dynamics and Flares, ed. S. Enome & T. Hirayama (Nobeyama Report 360), 123
Kosugi, T. 1994, in New Look at the Sun with Emphasis on Advanced Observations of Coronal Dynamics and Flares, ed. S. Enome & T. Hirayama (Nobeyama Report 360), 11
Kosugi, T., et al. 1991, Sol. Phys., 136, 17
LaRosa, T. N., Moore, R. L., Miller, J. A., & Shore, S. N. 1996, ApJ, 467, 454
Masuda, S. 1994a, Ph.D. thesis, National Astronomical Observatory, Univ. Tokyo
———. 1994b, in New Look at the Sun with Emphasis on Advanced Observations of Coronal Dynamics and Flares, ed. S. Enome & T. Hirayama (Nobeyama Report 360), 209
Masuda, S., Kosugi, T., Hara, H., Sakao, T., Shibata, K., & Tsuneta, S. 1995, PASJ, 47, 677
Masuda, S., Kosugi, T., Hara, H., Tsuneta, S., & Ogawara, Y. 1994, Nature, 371, 495
McTiernan, J. M., Kane, S. R., Hurley, K., Laros, J. G., Fenimore, E. E., Klebesadel, R. W., Sommer, M., & Yoshimori, M. 1994, in New Look at the Sun with Emphasis on Advanced Observations of Coronal Dynamics and Flares, ed. S. Enome & T. Hirayama (Nobeyama Report 360), 389
Miller, J. A., LaRosa, T. N., & Moore, R. L. 1996, ApJ, 461, 445
Moore, R. L., LaRosa, T. N., & Orwig, L. E. 1995, ApJ, 438, 985
Nakajima, H., et al. 1994, in New Look at the Sun with Emphasis on Advanced Observations of Coronal Dynamics and Flares, ed. S. Enome & T. Hirayama (Nobeyama Report 360), 185
Sakao, T. 1994, Ph.D. thesis, National Astronomical Observatory, Univ. Tokyo
Sakao, T., et al. 1992, PASJ, 44, L83
Sakao, T., Kosugi, T., Masuda, S., Yaji, K., Inda-Koide, M., & Makishima, K. 1994, in New Look at the Sun with Emphasis on Advanced Observations of Coronal Dynamics and Flares, ed. S. Enome & T. Hirayama (Nobeyama Report 360), 169
Shibata, K., Masuda, S., Shimojo, M., Hara, H., Yokoyama, T., Tsuneta, S., Kosugi, T., & Ogawara, Y. 1996, ApJ, 451, L83
Takano, T., & Nishio, M. 1995, private communication
Takakura, T., Inda, M., Makishima, K., Kosugi, T., Sakao, T., Masuda, S., Sakurai, T., & Ogawara, Y. 1993, PASJ, 45, 737
Takakura, T., Tanaka, K., & Hiei, E. 1984, Adv. Space Res., 4, 143
Tsuneta, S. 1996, ApJ, 456, 840
Tsuneta, S., et al. 1991, Sol. Phys., 136, 37
Wang, H., Gary, D. E., Zirin, H., Kosugi, T., Schwartz, R. A., & Linford, G. 1995a, ApJ, 444, L15
Wang, H., Gary, D. E., Zirin, H., Schwartz, R. A., Sakao, T., Kosugi, T., & Shibata, K. 1995b, ApJ, 453, 505
Wheatland, M. S., & Melrose, D. B. 1995, Sol. Phys., 158, 283
Wuelser, J. P., et al. 1994, ApJ, 424, 459
Yaji, K., Kosugi, T., Sakao, T., Masuda, S., Inda-Koide, M., & Hanaoka, Y. 1994, in New Look at the Sun with Emphasis on Advanced Observations of Coronal Dynamics and Flares, ed. S. Enome & T. Hirayama (Nobeyama Report 360), 143
Yoshimori, M., et al. 1992, PASJ, 44, L51
Zarro, D., Mariska, J. T., & Dennis, B. R. 1994, in New Look at the Sun with Emphasis on Advanced Observations of Coronal Dynamics and Flares, ed. S. Enome & T. Hirayama (Nobeyama Report 360), 221